Effect of Vortex Core Distortion on Blade-Vortex Interaction

D. J. Lee* and C. A. Smith†
NASA Ames Research Center, Moffett Field, California 94035

The effect of vortex distortion on the flow arising from the interaction of a convecting vortex and an airfoil is analyzed for two-dimensional, incompressible, inviscid flow. Significant distortion of the vortex structure, owing to interaction with the airfoil, can occur, especially during close interactions. The vorticity field is represented by multiple vortex elements. Vortex instability and diffusion, resulting from discretization in space and time, are discussed. An integral-boundary-element method is used to represent the airfoil surface and its effect on the flowfield. The body panels are redistributed on the surface as the vortices are convected past the airfoil to calculate the effect of the vorticity field more accurately. The method is applied to several cases to examine effects of vortex strength, distribution, and initial separation position. The distortion, even splitting, of the vortex core is observed for the case of close interaction. However, the extent of distortion depends strongly on the initial size and strength of the vortex. Also, the unsteady pressure term contributes significantly to both the surface-pressure distribution and total lift in addition to the quasisteady term. Circulation around the airfoil is also presented.

Nomenclature

A_{iv}	= ith vortex-element area
C_L	= $-\oint C_p \cdot n_y \, ds$
C_p	= $(p-p_\infty)/\frac{1}{2}\rho U^2$
c	= half-chord length
n	= unit outward normal vector at the airfoil surface
p	= surface pressure
p_∞	= freestream pressure
q_j	= jth source-panel strength
R_v	= oncoming vortex core radius/c
s	= tangential distance along the airfoil surface/c
t	= time · U/c
U	= magnitude of freestream velocity
u	= magnitude of flow velocity/U
x_v, y_v	= vortex position
Γ_a	= airfoil circulation/Uc
Γ_v	= oncoming vortex circulation/Uc
γ_a	= vortex panel strength
γ_{iv}	= ith vortex-element circulation/Uc

Introduction

BLADE-VORTEX interaction is a well-known phenomenon that occurs in the flowfield about a helicopter rotor; it is one of the primary sources of noise and vibration. In general, as shown in Fig. 1a, the induced velocity of the rotor disk tends to make all of the tip vortices pass under the rotor disk in level, steady-state flight. However, if the rotor operates in steady, descending flight, then the upflow tends to force the wake into the rotor disk, causing strong blade-vortex interactions. To study the flow during this interaction process, three regions should be considered: the convecting, or incident, vortex generated from a preceding blade; the flow about the blade surface interacting with the convecting vortex; and the wake shed from the blade during the interaction.

This flowfield is three dimensional, unsteady, viscous, and compressible. It has been studied by many researchers, both analytically and experimentally.[1,2] However, in previous studies, the emphasis was on the flow about the blade. The incident vortex was usually treated as a point vortex or as one with a fixed core that was not allowed to distort during the interaction. Distortion of the incident vortex owing to the interaction and the effects of the vortex distortion on the blade surface flow and aerodynamic characteristics have not been considered extensively until recently.

Reference 3 described an early two-dimensional model of this flow in which a point vortex is convected past an airfoil at a fixed half-chord separation distance. A later study examined the same problem, but allowed the vortex to move freely in response to the induced flowfield.[4] A fixed vortex core, using

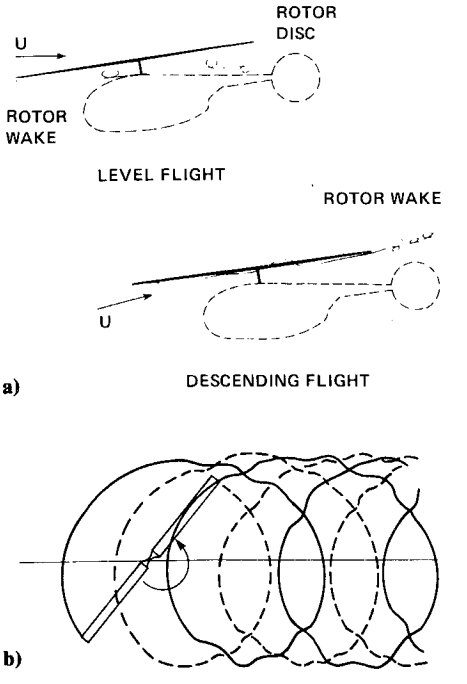

Fig. 1 Schematic of helicopter wake: a) side view; b) plan view (from Ref. 1).

Received Aug. 8, 1989; revision received Jan. 2, 1990; accepted for publication Jan. 2, 1990.

*NRC Fellow; currently, Assistant Professor, Department of Aerospace Engineering, Korea Advanced Inst. of Science and Technology, Seoul, Korea. Member AIAA.

†Executive Assistant to the Director. Member AIAA.

the Betz inviscid vortex model, was incorporated in Ref. 5. Each of these early studies encountered difficulties in modeling a close interaction because of the high velocities inside the vortex. In another study, close interactions were examined by using a finite-vortex core model having no singularity in the center; however, the effects of distortion were not examined.[6] More recent methods (e.g., Ref. 7) solve the problem by using finite-difference methods with a vortex having a finite core; however, the core itself is not allowed to distort.

The first attempt to model distortion of the core is described in Ref. 8. In that study, a finitie-difference solution to the incompressible Navier-Stokes equations was used. The Reynolds number was limited to values less than 200 because of the numerical scheme, and numerical diffusion of the vortex was not reported. A later study analyzed flow about a Joukowski airfoil in the presence of discrete vortices by using conformal mapping for quasisteady[9] and unsteady cases.[10] The most recent two-dimensional study including vortex distortion used a method that is fifth-order accurate in space to solve the thin-layer Navier-Stokes equation.[11] The solution required excessively fine grids to avoid numerical diffusion of the vortex core, which resulted in long computation times.

The present paper emphasizes the distortion of the vortex and its trajectory during blade-vortex interactions and its effect on the aerodynamic characteristics of the blade. The flow is assumed to be two dimensional, with the vortex axis parallel to the span of the blade (Fig. 1b).

The vorticity field is discretized as a region of multiple vortices, sometimes referred to as a vortex cloud. This discretization of the continuous vorticity field generally results in vortex diffusion and instability with the discretized time step. These problems and the techniques to minimize them are discussed in a later section. The vortices are tracked through the flowfield using Lagrangian techniques. An integral-panel method is used to represent the blade. To capture the effect of the vortex more accurately, the number, size, and location of the panels are redistributed as the vortex is convected past the airfoil.

This method is then applied to calculate the surface-pressure distributions and vortex trajectories at each time step and the lift and circulation around the airfoil as a function of time. It is also used to examine effects of vortex strength and size and vortex-blade initial separation position.

Mathematical Formulation

The flow geometry and coordinate definitions are given in Fig. 2. The flow is assumed to be two dimensional, unsteady, incompressible, inviscid, and rotational. The viscous effect is modeled by enforcing a zero pressure jump across the blade trailing edge at each time step. This determines the strength of the vorticity shed in the blade wake.

Unsteady, incompressible, inviscid, rotational flow in two dimensions can be expressed in vorticity ξ form as

$$\frac{\partial \xi}{\partial t} + \boldsymbol{u} \cdot \nabla \xi = 0 \tag{1}$$

where

$$\xi = \nabla \times \boldsymbol{u} \tag{2}$$

In the Lagrangian description (that is, when the flow is described in terms of flow particles moving with the velocity $\boldsymbol{u}$), Eq. (1) can be written as two separate equations for each $i\xi$th vorticity particle:

$$\frac{\partial \xi_{i\xi}(\boldsymbol{x},t)}{\partial t} = 0 \tag{3}$$

$$\frac{d\boldsymbol{x}_{i\xi}}{dt} = \boldsymbol{u} \tag{4}$$

This implies that the vorticity of each particle is not changed during the convection and that the total circulation in the flowfield is conserved in this inviscid assumption. The vorticity particles move with the local flow velocity.

The velocity field $\boldsymbol{u}$ is decomposed into a solenoidal field owing to vorticity in the flowfield $\boldsymbol{u}_\xi$ and an incompressible, irrotational, potential field $\boldsymbol{u}_\phi$:

$$\boldsymbol{u} = \boldsymbol{u}_\xi + \boldsymbol{u}_\phi \tag{5}$$

where

$$\nabla \cdot \boldsymbol{u}_\xi = 0, \qquad \nabla \times \boldsymbol{u}_\phi = 0 \tag{6}$$

The velocity $\boldsymbol{u}_\xi$ is obtained by solving a Poisson equation for the vector potential $\boldsymbol{A}$, derived from Eqs. (2) and (6)[12]:

$$\nabla^2 \boldsymbol{A} = -\xi \tag{7}$$

where

$$\boldsymbol{u}_\xi = \nabla \times \boldsymbol{A}$$

and the velocity $\boldsymbol{u}_\phi$ is obtained by solving the Laplacian equation for the scalar potential ϕ in incompressible flow as

$$\nabla^2 \phi = 0 \tag{8}$$

where

$$\boldsymbol{u}_\phi = \nabla \phi$$

The two fields are coupled through the normal boundary condition that there is no flow across the surface boundary:

$$\frac{\partial \phi}{\partial n} = -\boldsymbol{u}_\xi \cdot \boldsymbol{n} \tag{9}$$

The pressure on the surface can be obtained by using the unsteady Bernoulli equation, which is derived after integrating

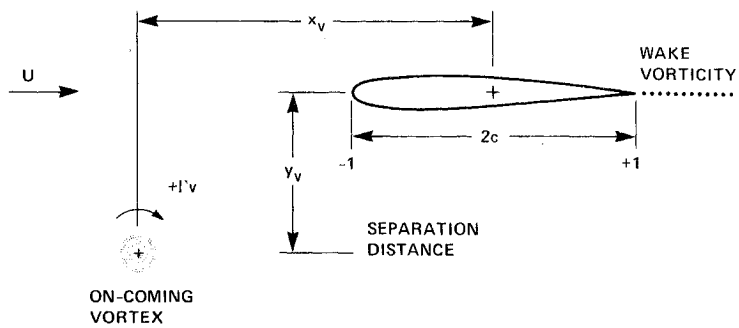

Fig. 2 Flow geometry.

the momentum equation along the streamline, as

$$C_p = 1 - u^2 - 2\frac{\partial \phi}{\partial t} - 2\int_s \frac{\partial u_\xi}{\partial t} \cdot ds \tag{10}$$

where u is the nondimensionalized total velocity and C_p is the pressure coefficient. The first two terms represent the quasi-steady pressure, and the last two terms represent the local unsteady pressure. The first of these unsteady terms is from the potential contribution, and the other is from the vorticity in the flow. The contributions from the steady pressure and the local unsteady pressure will be described later.

The total circulation in the flow, including the oncoming vortex Γ_v, the boundary layer around the airfoil Γ_a, and the wake Γ_w, is conserved:

$$\frac{d\Gamma(t)}{dt} = 0 \tag{11}$$

where

$$\Gamma(t) = \Gamma_a + \Gamma_v + \Gamma_w \tag{12}$$

and

$$\Gamma_a = \int_{\text{airfoil}} \boldsymbol{u} \cdot d\boldsymbol{s}, \qquad \Gamma_v = \iint \xi_v \cdot \boldsymbol{n}_s dS$$

$$\Gamma_w = \iint \xi_w \cdot \boldsymbol{n}_s dS \tag{13}$$

and $\boldsymbol{n}_s$ is the unit vector perpendicular to the vorticity area S.

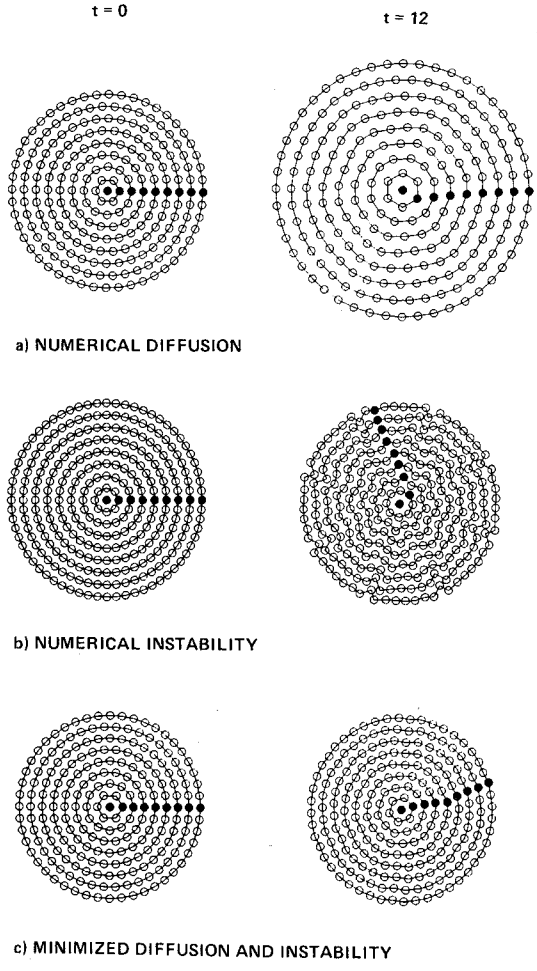

Fig. 3 Effects of numerical vortex diffusion and instability: $\Gamma_v = 0.4$, $R_v = 0.2$.

It is assumed that there is no pressure jump across the trailing edge at each time step. Using the unsteady Bernoulli equation [Eq. (10)], this gives

$$\frac{d\Gamma_a}{dt} = \frac{1}{2}\left(u^2_{\text{lower te}} - u^2_{\text{upper te}}\right) \tag{14}$$

An incident vortex of given strength is introduced at time $t = 0$ at a given position upstream of the blade

$$\xi = \xi(x_v, t = 0) \tag{15}$$

Vortex Model

The initial vorticity field in the vortex core is modeled as multiple, discrete, vortex elements, as shown in Fig. 2. Each vortex element has strength γ_{iv} representing the vorticity in the element area A_{iv} as

$$\gamma_{iv} = \int_{iv} \xi(x_{iv}, t = 0) dA_{iv} \tag{16}$$

The self-induced velocity component of the vortex cloud is obtained for an infinite domain from the Biot-Savart law, which is a solution of Eq. (7) for discrete vortices:

$$u_{\xi iv} = \Sigma_{jv} \frac{\gamma_{iv}(y_{jv} - y_{iv})}{2\pi \mid x_{iv} - x_{jv} \mid^2}, \quad v_{\xi iv} = \Sigma_{jv} \frac{-\gamma_{iv}(x_{jv} - x_{iv})}{2\pi \mid x_{iv} - x_{jv} \mid^2} \tag{17}$$

$$(iv \neq jv)$$

where $u_{\xi iv}$ and $v_{\xi iv}$ are the velocity components of the ith vortex element owing to the influence of all the other vortex elements.

The discretization of the continuous vortex core can lead to numerical instability and diffusion of the vortex with the discretized time step. Numerical diffusion is demonstrated in Fig. 3a for an isolated vortex convected through a uniform flowfield. Upon initial introduction into the flow, the vortex appears as on the left. The open symbols in Figs. 3 represent individual elements of the vortex cloud. The closed symbols are also individual vortex elements and are marked to show the rotation of the vortex cloud as it is convected. A time step (Δt) of 0.04 was used in this calculation. A Rankine vortex, having uniform vorticity in the core, is used as the initial vortex, and a first-order time scheme is employed for the calculation of the next position of the vortex elements. At $t = 12$, which corresponds to about 60 core radii of travel, numerical diffusion has increased the size of the vortex to that shown on the right. If no numerical instability and diffusion are present, the vortex at $t = 12$ would have a linear velocity profile, represented as a straight line of closed symbols in the radial direction, and the same radius of the vortex as that at $t = 0$.

A second-order, Runge-Kutta, time-integration method and more vortex elements have been used to prevent the diffusion, as shown in Fig. 3b. However, numerical instability occurs in this higher order integration. This is a result of initial disturbances induced by the discretized vortex elements. Therefore, to minimize this instability, the initial vortex is divided in such a way that each vortex element has an equal area A_{iv} and an aspect ratio (ratio of azimuthal length to radial length) close to one.

For the Rankine vortex, the equal area means equal circulation for each element. With these features, the instability can be reduced as shown in Fig. 3c. Each vortex element is also assumed to have a fixed core. The element core radius is determined so as to have the corresponding element area A_{iv}. Inside each vortex element the velocity depends on the core model used.[13,14] In all examples here, the velocity inside each core varies linearly with each vortex radius (i.e., solid-body rotation). This simple vortex-element model was used to enable us to focus on effects of vortex cloud size, strength, and

position relative to the airfoil. Higher order distributions of the individual vortex elements, although more representative, distribute the vorticity far from the center and thus create difficulties near a solid surface, and are beyond the scope of the present study. In future studies, the effect of the vortex-element model should be evaluated.

These multiple, discrete vortex elements are used for the interaction with the airfoil. The total strength of the vortex Γ_v is nondimensionalized by the half-chord length of the airfoil and freestream velocity U. The time step Δt is nondimensionalized by the freestream velocity and by the half-chord length. The initial upstream location of the vortex $x_v(x_v, y_v)$ and the radius R_v (see Fig. 2) are nondimensionalized by the half-chord length of the airfoil.

Solution Procedure

The governing equations [Eqs. (1) and (8)] are solved, subject to the boundary condition and auxiliary conditions, with the initial discretized vortex elements described in the previous section. The strength of the wake vortex, required to satisfy the trailing-edge condition and the conservation of circulation, is calculated and the vortex is shed into the wake as shown in Fig. 2. The shed wake also consists of discrete vortices having strengths γ_{iw}. The induced velocity owing to the wake $u_{\xi iw}$ is obtained from the Biot-Savart law. Next, the flow velocity at the location of all the vortices (i.e., incident vortex elements and wake vortex elements) is found. New positions of the vortices are calculated based on the local velocity. The vortices are moved to their new positions with the velocity

$$u_{iv,iw} = u_{\xi iv} + u_{\xi iw} + \nabla\phi \tag{18}$$

and the procedure is repeated.

A panel method is used to represent the body surface and to solve the potential satisfying the governing equation [Eq. (8)]

$$\phi(x_i,t) = U\cos(\alpha)x_i + U\sin(\alpha)y_i + \Sigma_j \frac{q_j(x_j,t)}{2\pi}\int_j \ln|x_i - x_j|\,ds_j + \frac{\gamma_a(t)}{2\pi} \times \Sigma_j \int_j \tan^{-1}\left(\frac{y_i - y_j}{x_i - x_j}\right) ds_j \tag{19}$$

where U is the freestream speed and α the airfoil angle of attack. The source strength $q_j(x_j,t)$ of each panel is uniform across the panel. The vortex-sheet strength is assumed to be uniform along the surface and is represented by $\gamma_a(t)$, circulation per unit length.[15]

By applying the normal boundary condition [Eq. (9)] at each surface panel, a set of linear equations for q_j and γ_a is obtained at each time step from Eqs. (11) and (17-19)

$$A_{ij}q_j + G_i\gamma_a = F_i \tag{20}$$

where A_{ij} and G_i are influence coefficients for q_j and γ_a, respectively. The term F_i is the normal velocity at the airfoil surface due to the freestream and vortices γ_{iv} and γ_{iw} in the vortex and wake regions, respectively.

By enforcing the trailing-edge boundary condition, a set of simultaneous, nonlinear, ordinary differential equations with time are obtained for γ_a (Γ_a per unit length) in Eq. (14) and for new positions of vortices $x_{iv,iw}$ in Eq. (4). Rather than an iteration scheme[15] for solving the nonlinear equation, a second-order, explicit, time-marching scheme is used for x_{iv}, and a first-order implicit scheme is used for γ_a:

$$x^{n+1}_{iv,iw} - x^n_{iv,iw} = \tfrac{1}{2}\left(u^{n+\frac{1}{2}}_{iv,iw} + u^n_{iv,iw}\right)\cdot\Delta t \tag{21}$$

$$\gamma^{n+h}_a - \gamma^n_a = \tfrac{1}{2}\{(u^{n+h})^2_{\text{lower te}} - (u^{n+h})^2_{\text{upper te}}\}\cdot\Delta t/\oint ds \tag{22}$$

where $u^{\tilde{n}}_{iv,iw}$ is the velocity of vortices calculated at the location

$$x^{n+\frac{1}{2}}_{iv,iw} = x^n_{iv,iw} + u^n_{iv,iw}\cdot\Delta t \tag{23}$$

where the superscripts designate time steps, and $h = 1/2$ for the predictor and $h = 1$ for the corrector. To calculate the location of the newly shed vortex element $x^{n+\frac{1}{2}}_{iw}$ in Eq. (23) for the predictor, the convecting velocity u^n_{iw} is taken as half the local velocity at a distance equal to the radius of the wake vortex element from the trailing edge along the line of the bisection of the trailing-edge angle. The final location x^{n+1}_{iw} is determined from Eq. (21). The tangential velocity, u^{n+h} in Eq. (22), is obtained from Eqs. (8) and (19) for the velocity u_ϕ and from the Biot-Savart law for the velocity u_ξ. The source strength q_j in Eq. (19) can be expressed in terms of γ^{n+h}_a using Eq. (20), and the strength of the newly shed vortex is also directly related to γ^{n+h}_a. Then Eq. (22) becomes a quadratic equation for γ^{n+h}_a, which can be solved analytically. Once γ^{n+h}_a is obtained, q_j, u, and C_p are obtained.

The solution is quite sensitive to panel size, number, and location relative to the incident vortex. As a vortex gets very near a surface, it becomes difficult to resolve the large velocity gradients with only a few panels near the vortex. A general method is utilized here; it determines the panel size, number, and positions for multiple vortices moving around the airfoil. More panels are located in regions of large gradients in the normal velocity. As the vortex is convected along the surface, the region of dense panel spacing also moves. An example of this technique, applied to a fixed vortex located near the rear of the airfoil, was shown in Ref. 16.

Results and Discussion

Using the solution technique described in the previous section, two representative cases will be analyzed. The first is an unsteady airfoil-vortex interaction, with the vortex represented as a single potential vortex in a way similar to that used in previous studies. The second is the unsteady airfoil-vortex interaction with multiple vortices representing the incident vortex. The airfoil has a NACA 0012 profile and is at zero angle of attack relative to the freestream.

Potential Vortex Model

An unsteady, two-dimensional, airfoil-vortex interaction is first calculated with the incident vortex represented by a single potential vortex. This is a classic problem that has been treated many times before for Joukowski airfoils.[4,17] It is included here so that effects of distortion of the incident vortex field can be better evaluated, as can the adaptive-panel-distribution technique for modeling the arbitrary airfoil shape. In the

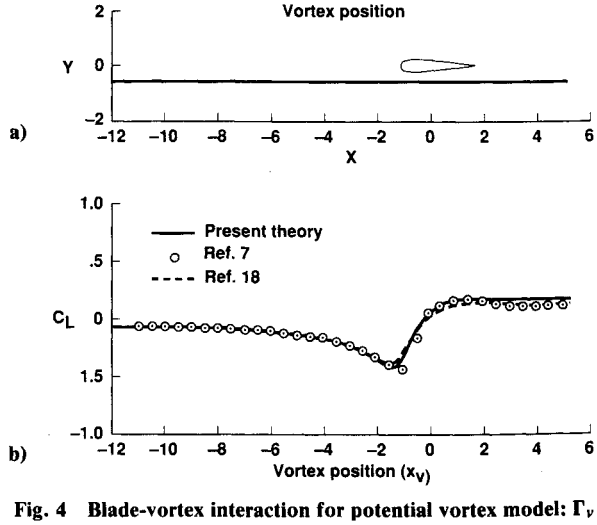

Fig. 4 Blade-vortex interaction for potential vortex model: $\Gamma_v = 0.4$, $y_v = -0.52$.

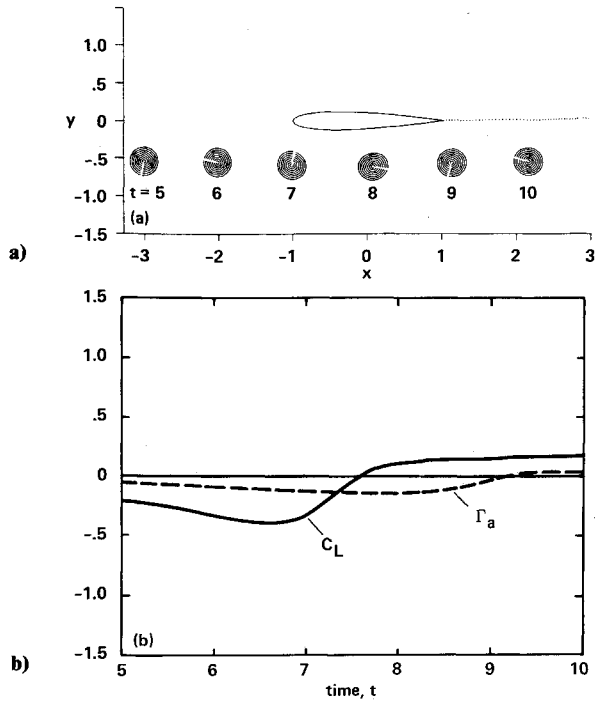

Fig. 5 Blade-vortex interaction for distributed vortex model: $\Gamma_v = 0.4$, $y_v = -0.52$, $R_v = 0.2$: a) vortex trajectory; b) airfoil force.

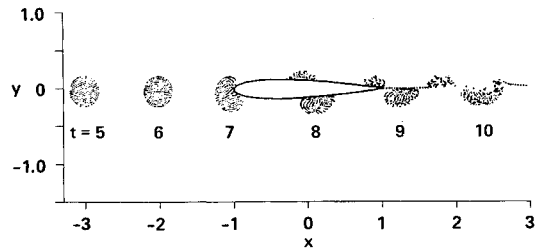

Fig. 6 Blade-vortex interaction for zero vertical separation distance-vortex trajectory: $\Gamma_v = 0.4$, $y_v = 0.0$, $R_v = 0.2$.

examples shown here, the wake shed from the airfoil is allowed to distort and interact with the incident vortex. This has not been included in most previous analyses.

The example, given in Figs. 4, shows the vortex trajectory and unsteady lift ($\Gamma_v = 0.4$ $y_v = -0.52$, and $x_v = -8$) and compares the results of the present work with similar results from Refs. 7 and 18. There is a continuous decrease in lift as the vortex approaches the airfoil, followed by a significant increase as the vortex passes the airfoil leading edge for this large separation distance. There is no corresponding change in lift as the vortex passes the trailing edge. Effects of vertical separation distance on the vortex trajectory, airfoil unsteady lift, and circulation around the airfoil Γ_a were shown in Ref. 16. As the separation distance is decreased, the change in lift as the vortex nears the leading edge becomes steeper; there is also a change in lift as the vortex passes the trailing edge. This change in lift as the vortex passes the trailing edge has not been seen experimentally.[19] This will be elaborated upon later.

Distributed Vortex Model

The first example to be described with the oncoming vortex represented by multiple vortices (also referred to as a distributed vortex) is the same interaction modeled in Figs. 4 for a potential vortex. Results using the distributed vortex (core radius $R_v = 0.2$, strength $\Gamma_v = 0.4$, and angle of attack $\alpha = 0$ deg) are shown in Fig. 5a. This size vortex relative to the airfoil is chosen because it is representative of those occurring in the helicopter blade-vortex-interaction problem. Also, it produces the nonlinear interaction being modeled. Initially, the vortex is released at $x_v = -8$ and the positions are calculated with time step $\Delta t = 0.04$. For this separation distance, $y_v = -0.52$, the core remains quite stable during the interaction, and there is negligible distortion. The airfoil lift is very similar to the lift using a potential vortex (Fig. 4b). For the case of this distributed vortex, the lift is plotted as a function of time instead of vortex position used for the case of the point vortex. Shown in Fig. 5b is the circulation around the airfoil during the interaction.

Results for zero vertical-separation distance using the distributed-vortex model are shown in Figs. 6–9. Initial conditions for the vortex are the same as those for the large separa-

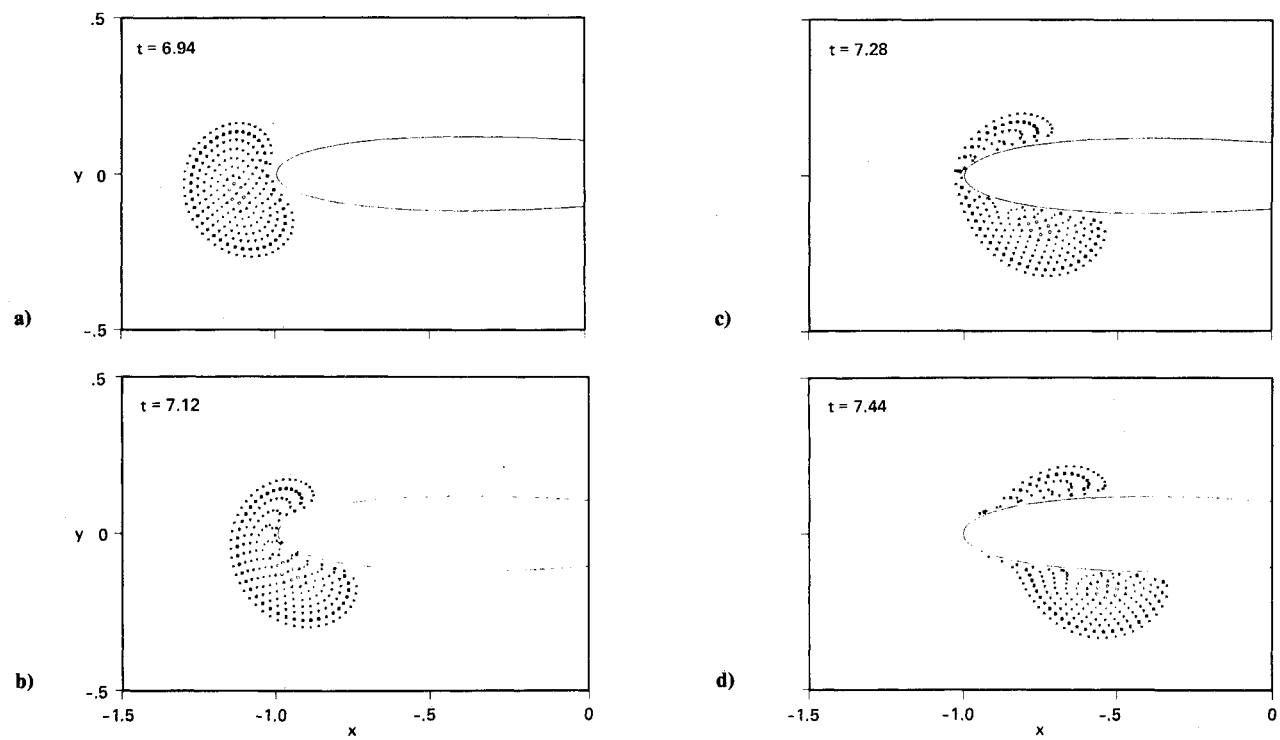

Fig. 7 Blade-vortex interaction for zero vertical separation distance-vortex distortion at leading edge: $\Gamma_v = 0.4$, $y_v = 0.0$, $R_v = 0.2$.

tion distance, except $y_v = 0$. There is substantial distortion and even splitting of the vortex as it interacts with the airfoil. This is shown in Fig. 6, which shows the vortex at several discrete times as it nears, and is convected past, the leading edge with different velocities on the upper and lower surface of the airfoil, as indicated in Figs. 6 and 7. After the vortex passes the trailing edge, there is significant mixing with the airfoil wake. A closeup of the shearing of the vortex into separate components at the airfoil leading edge is shown in Fig. 7. Similar distortion is also seen in flow-visualization studies.[20,21] Viscous effects, although not modeled here, are not expected to be significant, especially at high Reynolds number. In real flows, such as the helicopter case, the speed at which the interaction occurs, the strength of the vortex, and its proximity to the airfoil combine to make the interaction primarily inviscid. Also, as in the case being studied here, the relatively large leading-edge radius and the airfoil thickness prevent leading-edge separation for a weak oncoming vortex. Viscous calculations at high Reynolds number[11] also show no significant viscous effects.

Forces on the airfoil (Figs. 8) indicate both a larger lift owing to the interaction and a steeper slope, likely resulting in greater noise propagation into the far field for this interaction. The trailing-edge lift variation, observed for the potential vortex[16] for zero separation distance, is not shown for this distributed vortex. However, this depends on the strength and size of the vortex, as shown later. The lift is decomposed in Fig. 8b into the quasisteady terms and the unsteady terms [the

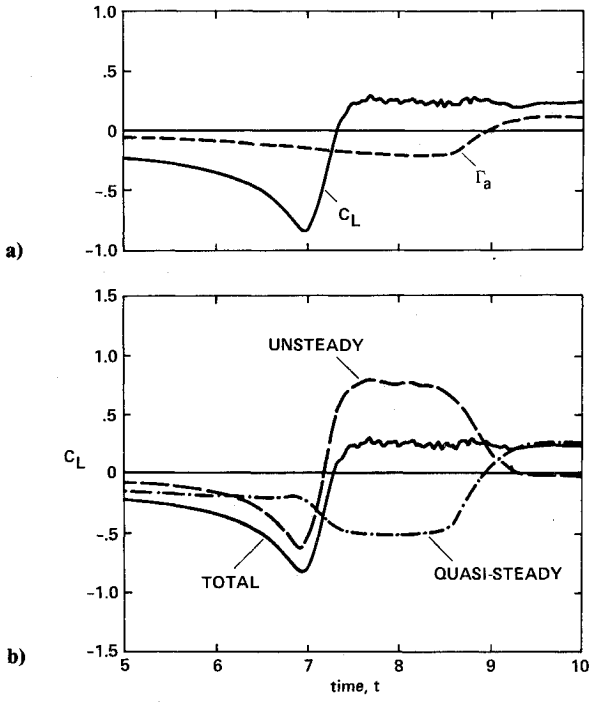

Fig. 8 Blade-vortex interaction for zero vertical separation distance-airfoil force: $\Gamma_v = 0.4$, $y_v = 0.0$, $R_v = 0.2$.

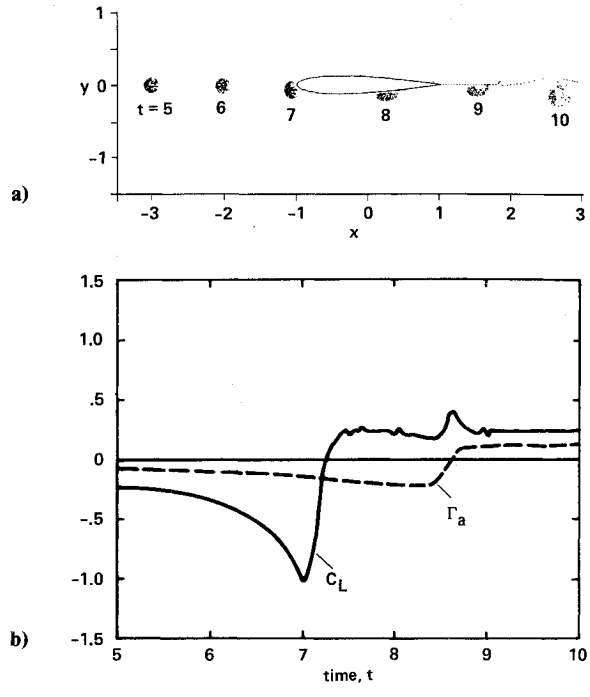

Fig. 10 Effect of smaller vortex size: $\Gamma_v = 0.4$, $y_v = 0.0$, $R_v = 0.1$: a) vortex trajectory; b) airfoil force.

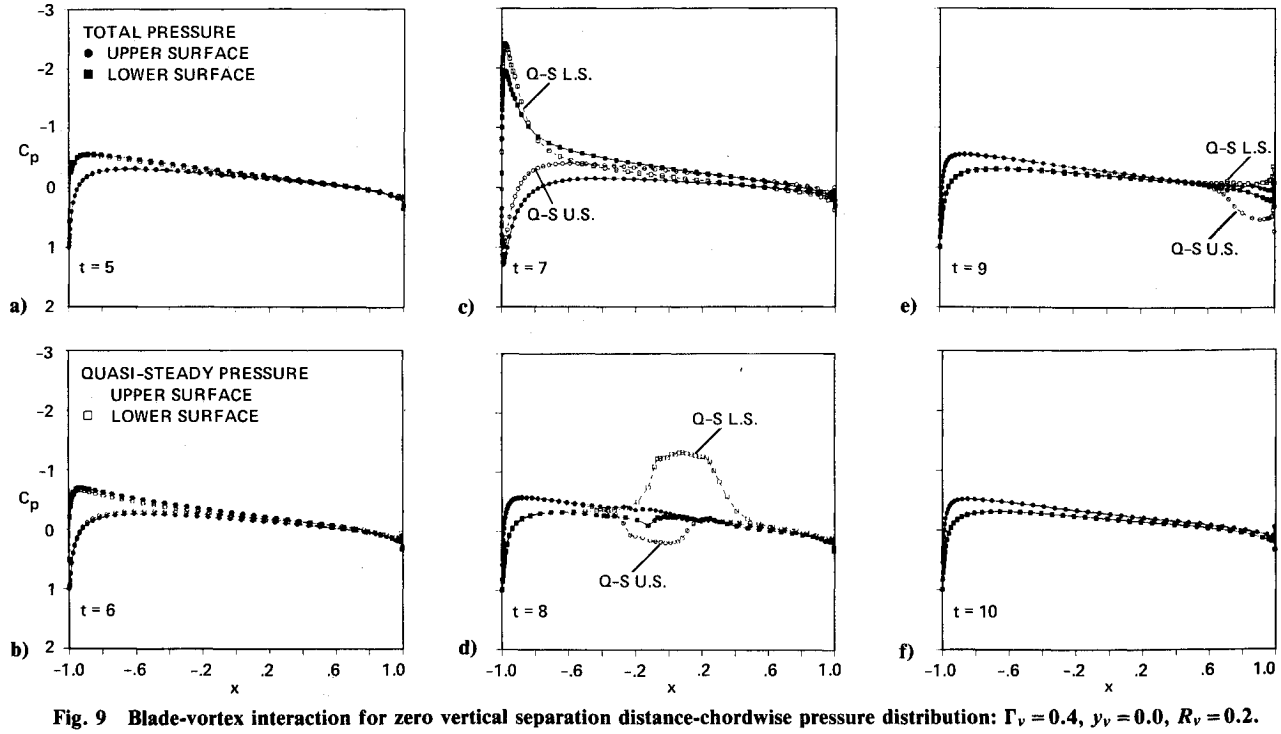

Fig. 9 Blade-vortex interaction for zero vertical separation distance-chordwise pressure distribution: $\Gamma_v = 0.4$, $y_v = 0.0$, $R_v = 0.2$.

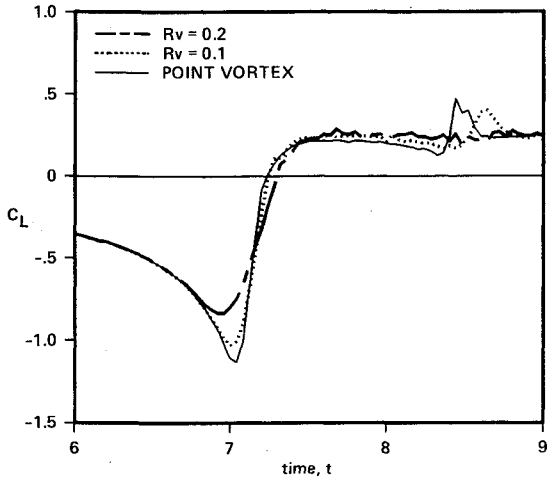

Fig. 11 Effect of vortex size on airfoil lift coefficient: $\Gamma_v = 0.4$, $y_v = 0.0$.

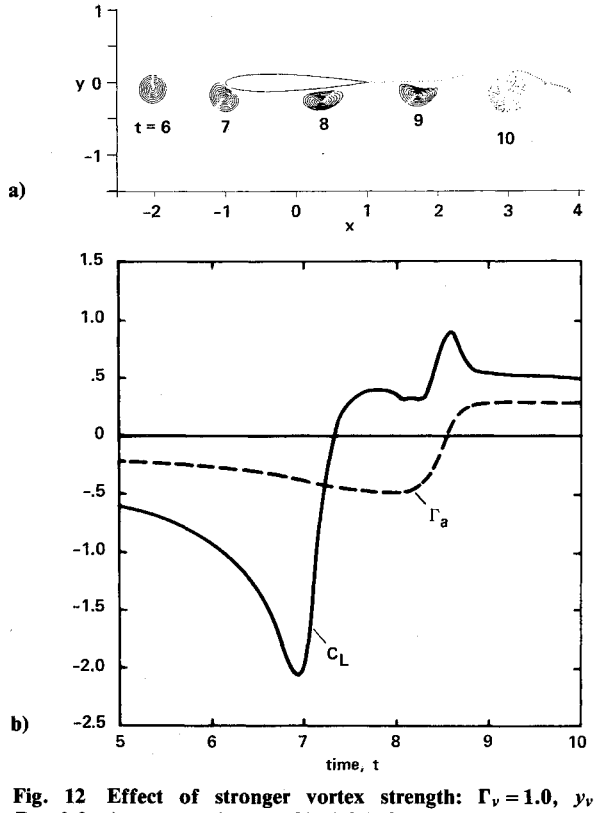

Fig. 12 Effect of stronger vortex strength: $\Gamma_v = 1.0$, $y_v = 0.0$, $R_v = 0.2$: a) vortex trajectory; b) airfoil force.

first two terms and the last two terms of Eq. (10), respectively]. Although the two components (quasisteady and unsteady) are similar in magnitude, the variation in total lift is due primarily to the variation in the unsteady lift. It is this variation in lift (i.e., dL/dt) that is responsible for blade-vortex interaction noise. Thus, it is important that the full, unsteady Bernoulli equation be used in calculations.

The chordwise pressure distribution shown in Fig. 9 (corresponding to the discrete time steps shown in Fig. 6) shows another interesting effect. When the full, unsteady Bernoulli equation is used to calculate the pressure, a sharp pressure fluctuation is observed only at the leading edge, as has been observed in experiments.[22] Interestingly, however, if only the quasisteady pressure terms from Eq. (10) are used, the pressure fluctuation propagates all along the airfoil as the vortex is convected past. (The very small, local fluctuations in C_p as the vortex is convected past the airfoil are due to the discretized, concentrated vortex elements near the surface.)

Distortion of the vortex, as well as the lift on the airfoil, is dependent on the size and strength of the oncoming vortex. If a vortex half the size of the one in Figs. 6–9 is used (while maintaining the same strength), the vortex itself does not split as a result of the interaction with the airfoil, as shown in Figs. 10. The lift and the gradient of the lift increase with the smaller vortex. In addition, the smaller vortex produces a distinct change in lift as it passes the airfoil trailing edge (unlike that seen in Figs. 8). This is because the velocity induced by a concentrated vortex is much higher than the velocity induced by a distributed vortex. The change in circulation with time (shown in Fig. 10b) indicates that at the beginning of the interaction the shed wake is weak. However, when the vortex passes the trailing edge, a stronger wake is shed due to the rapid change in the circulation. After the vortex passes the trailing edge at these close separation distances, a strong interaction with the airfoil wake occurs. This results in wake roll up or mixing, depending on the signs and strengths of the two vortex fields.

The effect of the vortex size is clearly shown in Fig. 11 by comparing the lift due to a point vortex, the smaller distributed vortex, and the larger one. The amplitude and gradient of the lift, when the vortex nears the leading edge of the airfoil, increase as the vortex size decreases. The fluctuation in lift as the vortex passes the trailing edge also increases as the vortex size decreases. The trailing-edge fluctuations also indicate that the point vortex convects faster than the distributed vortex.

Effects of increasing the vortex strength are presented in Figs. 12. Here, a vortex 2.5 times as strong as that used in Figs. 6–9 is used, but the radius is not changed. In this case, the vortex does not split into separate components, but is distorted as it convects past the airfoil. This stronger vortex also produces a trailing-edge lift variation, as was seen in the previous case where the strength was held constant, but the size was reduced. Although the vortex is not split, there is still significant mixing with the shed wake of the airfoil after the vortex passes the trailing edge.

Conclusions

Distortion of the vortex during two-dimensional, blade-vortex interaction is investigated using distributed discrete vortices and an adaptive panel distribution. This method permits close interactions between a vortex and a lifting surface to be studied. It is shown that significant distortion of the vortex, and even splitting, can occur during close interactions. The amount of vortex distortion, airfoil lift, and mixing of the vortex with the airfoil wake are strongly dependent on the strength and size of the vortex. For the same separation distance, the vortex having the weaker strength or a larger size is more likely to be split. In most cases, there is a rapid variation in both surface pressure and total lift when the vortex nears the airfoil leading edge. However, the stronger or smaller vortex also causes a distinct change in lift when the vortex passes the trailing edge. In addition, the unsteady pressure terms play a significant role in the lift variation during the interaction. Additional investigations of the effects of airfoil profile, airfoil angle of attack, and vortex structure, especially during close interactions, are planned for the future.

Acknowledgment

This work was done while the first author held a National Research Council (NASA Ames Research Center) Research Associateship.

References

[1]Schmitz, F. H., and Yu, Y. H., "Helicopter Impulsive Noise: Theoretical and Experimental Status," *Recent Advances in Aeroacoustics*, edited by A. Krothapalli and C. A. Smith, Springer-Verlag, New York, 1986.

[2]U.S. Army Research Office Workshop on Blade Vortex Interac-

tions, NASA Ames Research Center, Moffett Field, CA, Oct. 1984.
[3]Sears, W. R., "Aerodynamics, Noise, and the Sonic Boom," *AIAA Journal,* Vol. 7, No. 4, 1969, pp. 557–586.
[4]Parthasarthy, R., and Karamcheti, K., "Aerodynamic Sound Generation Due to Vortex-Airfoil Interaction," AIAA Paper 73-224, Jan. 1973.
[5]Widnall, E. S., and Wolf, T. L., "Effect of Tip Vortex Structure on Helicopter Noise Due to Blade-Vortex Interaction," *Journal of Aircraft,* Vol. 17, No. 10, 1980, pp. 705–711.
[6]Lee, D. J., and Roberts, L., "Interaction of a Turbulent Vortex with a Lifting Surface," AIAA Paper 85-0004, Jan. 1985.
[7]Srinivasen, G. R., and McCroskey, W. J., "Computations of Blade-Vortex Interaction by Different Methods," U.S. Army Research Office Workshop on Blade Vortex Interactions, NASA Ames Research Center, Moffett Field, CA, Oct. 1984.
[8]Hardin, J. C., and Lamkin, S. L., "Aeroacoustic Interaction of a Distributed Vortex with a Lifting Joukowski Airfoil," AIAA Paper 84-2287, Oct. 1984.
[9]Panaras, A., "Numerical Modeling of the Vortex/Airfoil Interaction," *AIAA Journal,* Vol. 25, No. 1, 1987, pp. 5–11.
[10]Poling, D. R., Wilder, M. C., and Telinois, D. P., "Two-Dimensional Interaction of Vortices with a Blade," AIAA Paper 88-0044, Nov. 1988.
[11]Rai, M. M., "Navier-Stokes Simulations of Blade-Vortex Interaction Using High-Order Accurate Upwind Schemes," AIAA Paper 87-0543, Nov. 1987.
[12]Karamcheti, K., *Principles of Ideal-Fluid Aerodynamics,* Wiley, New York, 1966.
[13]Deffenbaugh, F. D., and Shivanada, T. E., "Discrete Vortex Wake Modeling of Separated Flow Phenomena," Rept. 33945-6001-UT-00 TRW, Inc., Aug. 1980.
[14]Chorin, A. J., "Numerical Study of Slightly Viscous Flow," *Journal of Fluid Mechanics,* Vol. 57, Pt. 4, 1973, pp. 785–796.
[15]Basu, B. C., and Hancock, G. J., "The Unsteady Motion of a Two-Dimensional Aerofoil in Incompressible Inviscid Flow," *Journal of Fluid Mechanics,* Vol. 87, Pt. 1, 1978, pp. 159–178.
[16]Lee, D. J., and Smith, C. A., "Distortion of the Vortex Core During Blade-Vortex Interaction," AIAA Paper 87-1243, June 1987.
[17]Chow, C. Y., and Huang, M. K., "Unsteady Flows about a Joukowski Airfoil in the Presence of Moving Vortices," AIAA Paper 83 0129, Jan. 1983.
[18]Wu, J. C., Sankar, N. L., and Hsu, T. M. "Unsteady Aerodynamics of an Airfoil Encountering a Passing Vortex," AIAA Paper 85-0203, Jan. 1985.
[19]Caradonna, F. X., Laub, G. H., and Tung, C., "An Experimental Investigation of the Parallel Blade-Vortex Interaction," 10th European Rotorcraft Forum, The Hague, The Netherlands, Aug. 1984.
[20]Ziada, S., and Rockwell, D., "Vortex-Leading Edge Interaction," *Journal of Fluid Mechanics,* Vol. 118, 1982, pp. 79–107.
[21]Yu, J. C., "Flow-Field Visualization of Two-Dimensional Blade-Vortex Encounters," U.S. Army Research Office Workshop on Blade-Vortex Interaction, Ames Research Center, Moffett Field, CA, Oct. 1984.
[22]Shockey, G. A., Williamson, J. W., and Cox, C. R., "Helicopter Aerodynamics and Structural Loads Survey," American Helicopter Society, Paper 1060, May 1976.